JOURNAL OF COMPUTATIONAL PHYSICS 109, 16-29 (1993)

Transport of Gyration-Dominated Space Plasmas of Thermal Origin 2: Numerical Solution

Á. KŐRÖSMEZEY,* C. E. RASMUSSEN, AND T. I. GOMBOSI

Space Physics Research Laboratory, Department of Atmospheric, Oceanic and Space Sciences, University of Michigan, Ann Arbor, Michigan 48109-2143

AND

BRAM VAN LEER

Department of Aerospace Engineering, University of Michigan, Ann Arbor, Michigan 48109-2140

Received June 8, 1992; revised February 1, 1993

A numerical solution has been found for the hyperbolic initial-value problem, which follows from the 16-moment set of equations describing the transport of a plasma in a strong magnetic field. In addition to the time-dependent evolution of mass and momentum, these equations describe the variations in anisotropic temperatures and heat fluxes for both ion and electron species. The numerical solution employs a high-order Godunov method to achieve third-order accuracy in space and second-order accuracy in time. The method includes an approximate Riemann solver which is suitable for a system of equations that cannot entirely be expressed in conservation form. In addition, a new technique has been developed to overcome the stiffness that occurs in regions where plasma flows are strongly reactive. Simple test cases showing correct wave behavior are presented.

1. INTRODUCTION

This paper is a continuation of [6], where our basic equations are derived and their relevance in solving problems in space plasma physics is demonstrated. These transport equations are sufficiently different from standard hydrodynamic or magnetohydrodynamic equations to require special numerical treatment. Here we present a numerical scheme to solve the equations. The paper is self-contained; it can be understood without the knowledge of [6].

A magnetized plasma generally has a large number of degrees of freedom. It therefore comes as no surprise that equations describing the transport of a plasma can appear intractable. This is especially apparent in regions where collisions between particles are infrequent. In this instance, species distribution functions can depart significantly from a Maxwellian; hence, low-order hydrodynamic equations are no longer applicable. To overcome this deficiency, generalized transport equations have been developed; see, e.g., [1, 2]. These transport equations retain the continuum approach of the hydrodynamic equations but expand the set of equations to include anisotropic pressures and heat fluxes.

These higher-order transport equations are so complicated that a general three-dimensional solution, analytical or numerical, has never been attempted. Two common sets of higher-order transport equations are based on 16 and 20 moments, respectively, of Boltzmann's equation. Thus, the 20-moment set includes 20 coupled, time-dependent partial-differential equations for each plasma species; see, e.g., [3]. The 16-moment set (see, e.g., [4, 5]) is based on a bi-Maxwellian distribution function and includes 16 coupled equations for each plasma species.

Considerable simplification of the higher-order equations occurs whenever the magnetic field is very large; see, e.g., [6]. In this instance, the magnetic field restrains plasma flows to follow magnetic field lines, so solutions to the transport equations become one-dimensional in character. This simplification of the 16-moment set of transport equations has allowed numerical solutions to be attempted by Khazanov *et al.* [7] and Mitchell and Palmadesso [8]. Unfortunately, these models have encountered numerical difficulties, ranging from stiffness to instability. It has been suggested that some of these problems may occur as a result of the truncation of the infinite system of coupled transport equations used to derive the 16-moment set [9].

In this paper we describe a numerical model to solve the hyperbolic initial-value problem that follows from the 16-moment set of transport equations in a strong magnetic field. This new model uses a generalization of the characteristic-based method developed by Godunov [10] and later extended by Van Leer [11, 12] to achieve third-order

* On leave from Central Research Institute for Physics, Budapest, 1525, Hungary.

0021-9991/93 $5.00

accuracy in space and second-order accuracy in time. A fundamental building block of Godunov-type methods is the technique to solve the Riemann problem describing the interaction of neighboring computational cells. The present method includes a new modification of the "approximate Riemann solver" of Roe [13], suitable for a system of equations that cannot entirely be expressed in conservation form. In addition, a new technique has been developed to overcome the stiffness that occurs in regions where plasma flows are strongly reactive. The overall method appears to be free of the numerical instabilities in the heat fluxes reported by Palmadesso *et al.* [9].

In the next section we describe the set of plasma transport equations that have been solved numerically. These equations describe a plasma consisting of ions of a single species and electrons, although the numerical method described in Section 3 can be generalized to include multiple ion species. In Section 4 some numerical solutions to the transport equations are presented which clearly show the propagation of ion waves through the plasma. The results presented in the paper are summarized in the concluding section.

2. TRANSPORT EQUATIONS

We seek a one-dimensional numerical solution to the set of transport equations given by Gombosi and Rasmussen [6] along a magnetic field line. These equations can be written in the non-conservative form,

$$\frac{D_\perp \mathbf{w}}{Dt} + \mathbf{A}\frac{\partial \mathbf{w}}{\partial x} = \mathbf{S} = \mathbf{S}_B + \mathbf{S}_{v_\perp} + \mathbf{S}_c, \tag{1}$$

where t is time, x is distance in the direction of the magnetic field $\mathbf{B}$, and the operator, $D_\perp/Dt = \partial/\partial t + \mathbf{u}_\perp \cdot \nabla$, is the total time derivative for an element of plasma drifting perpendicular to $\mathbf{B}$ with velocity $\mathbf{u}_\perp$ (∇ denotes differentiation in the perpendicular direction). In the case of strong magnetic fields, plasma movement perpendicular to the field line is small compared to the parallel movement; therefore, terms describing perpendicular transport can be treated as source terms. The drift velocity $\mathbf{u}_\perp$ and spatial derivatives in the perpendicular direction are assumed to be given for a specific problem. The elements of the vector $\mathbf{w}(x, t)$ are

$$\mathbf{w}(x,t) = \left(\frac{\rho}{B}, u, \frac{p_{i\parallel}}{B}, \frac{q_{i\parallel}}{B}, \frac{p_{i\perp}}{B}, \frac{q_{i\perp}}{B}, \frac{p_{e\parallel}}{B}, \frac{q_{e\parallel}}{B}, \frac{p_{e\perp}}{B}, \frac{q_{e\perp}}{B}\right)^T, \tag{2}$$

where ρ is mass density, u is bulk velocity, p is partial pressure, and q is heat flux. The subscripts i and e refer to the ion and electron species while the subscripts $\parallel$ and $\perp$ represent the parallel and perpendicular component to B, respectively. The components of the matrix $\mathbf{A}(x, t)$ are

$$\mathbf{A}(x,t) = \begin{bmatrix}
u & \frac{\rho}{B} & 0 & 0 & 0 & 0 & 0 & 0 & 0 & 0 \\
0 & u & \frac{B}{\rho} & 0 & 0 & 0 & \frac{B}{\rho} & 0 & 0 & 0 \\
0 & 3\frac{p_{i\parallel}}{B} & u & 1 & 0 & 0 & 0 & 0 & 0 & 0 \\
-3c_{i\parallel}^4 & 4\frac{q_{i\parallel}}{B} & 3c_{i\parallel}^2 & u & 0 & 0 & 0 & 0 & 0 & 0 \\
0 & \frac{p_{i\perp}}{B} & 0 & 0 & u & 1 & 0 & 0 & 0 & 0 \\
-c_{i\parallel}^2 c_{i\perp}^2 & 2\frac{q_{i\perp}}{B} & 0 & 0 & c_{i\parallel}^2 & u & 0 & 0 & 0 & 0 \\
0 & 3\frac{p_{e\parallel}}{B} & 0 & 0 & 0 & 0 & u & 1 & 0 & 0 \\
-3\chi c_{e\parallel}^4 & 4\frac{q_{e\parallel}}{B} & 0 & 0 & 0 & 0 & 3c_{e\parallel}^2 & u & 0 & 0 \\
0 & \frac{p_{e\perp}}{B} & 0 & 0 & 0 & 0 & 0 & 0 & u & 1 \\
-\chi c_{e\parallel}^2 c_{e\perp}^2 & 2\frac{q_{e\perp}}{B} & 0 & 0 & 0 & 0 & 0 & 0 & c_{e\parallel}^2 & u
\end{bmatrix}, \tag{3}$$

where χ is the electron to ion mass ratio m_e/m_i and c represents the various thermal speeds; for example, $c_{i\parallel} = \sqrt{p_{i\parallel}/\rho}$ is the parallel component of the ion thermal speed while $c_{e\perp} = \sqrt{p_{e\perp}/\rho/\chi}$ is the perpendicular component of the electron thermal speed.

The terms on the right-hand side of (1) represent source terms and have been grouped into three components. The first of these source-term vectors is

$$\mathbf{S}_B(x,t) = \begin{bmatrix}
0 \\
-(c_{i\perp}^2 + \chi c_{e\perp}^2)\frac{1}{B}\frac{\partial B}{\partial x} \\
-2\frac{q_{i\perp}}{B}\frac{1}{B}\frac{\partial B}{\partial x} \\
0 \\
\frac{up_{i\perp} + q_{i\perp}}{B}\frac{1}{B}\frac{\partial B}{\partial x} \\
\frac{uq_{i\perp} + c_{i\perp}^2(p_{i\parallel} - p_{i\perp})}{B}\frac{1}{B}\frac{\partial B}{\partial x} \\
-2\frac{q_{e\perp}}{B}\frac{1}{B}\frac{\partial B}{\partial x} \\
0 \\
\frac{up_{e\perp} + q_{e\perp}}{B}\frac{1}{B}\frac{\partial B}{\partial x} \\
\frac{uq_{e\perp} + c_{e\perp}^2(p_{e\parallel} - p_{e\perp})}{B}\frac{1}{B}\frac{\partial B}{\partial x}
\end{bmatrix} \tag{4}$$

and represents the effects of variations in the cross-sectional area (proportional to $1/B$) of the confining tube of magnetic flux. The second source term in (1),

$$\mathbf{S}_{u_\perp}(x,t)=\begin{pmatrix} -\frac{\rho}{B}\left(\frac{1}{B}\frac{D_\perp B}{Dt}+\nabla\cdot\mathbf{u}_\perp\right) \\ \mathbf{u}_\perp\cdot\left(\frac{D_\perp}{Dt}+u\frac{\partial}{\partial x}\right)\left(\frac{\mathbf{B}}{B}\right) \\ -\frac{p_{i\|}}{B}\left(\frac{1}{B}\frac{D_\perp B}{Dt}+\nabla\cdot\mathbf{u}_\perp-2\frac{\mathbf{u}_\perp\cdot\mathbf{R}}{R^2}\right) \\ -\frac{q_{i\|}}{B}\left(\frac{1}{B}\frac{D_\perp B}{Dt}+\nabla\cdot\mathbf{u}_\perp-3\frac{\mathbf{u}_\perp\cdot\mathbf{R}}{R^2}\right) \\ -\frac{p_{i\perp}}{B}\left(\frac{1}{B}\frac{D_\perp B}{Dt}+2\nabla\cdot\mathbf{u}_\perp+\frac{\mathbf{u}_\perp\cdot\mathbf{R}}{R^2}\right) \\ -\frac{q_{i\perp}}{B}\left(\frac{1}{B}\frac{D_\perp B}{Dt}+2\nabla\cdot\mathbf{u}_\perp\right) \\ -\frac{p_{e\|}}{B}\left(\frac{1}{B}\frac{D_\perp B}{Dt}+\nabla\cdot\mathbf{u}_\perp-2\frac{\mathbf{u}_\perp\cdot\mathbf{R}}{R^2}\right) \\ -\frac{q_{e\|}}{B}\left(\frac{1}{B}\frac{D_\perp B}{Dt}+\nabla\cdot\mathbf{u}_\perp-3\frac{\mathbf{u}_\perp\cdot\mathbf{R}}{R^2}\right) \\ -\frac{p_{e\perp}}{B}\left(\frac{1}{B}\frac{D_\perp B}{Dt}+2\nabla\cdot\mathbf{u}_\perp+\frac{\mathbf{u}_\perp\cdot\mathbf{R}}{R^2}\right) \\ -\frac{q_{e\perp}}{B}\left(\frac{1}{B}\frac{D_\perp B}{Dt}+2\nabla\cdot\mathbf{u}_\perp\right) \end{pmatrix}, \tag{5}$$

represent sthe effect of changes in the volume of the tube of plasma, due to plasma drifts in a plane perpendicular to the magnetic field, where **R** is the radius vector of magnetic field curvature. Finally, the third source term in (1),

$$\mathbf{S}_c(x,t)=\begin{pmatrix} \frac{\dot\rho}{B} \\ \frac{\dot M_{i\|}+\dot M_{e\|}}{B} \\ \frac{\dot p_{i\|}}{B} \\ \frac{\dot q_{i\|}}{B}-3c_{i\|}^2\frac{\dot M_{i\|}}{B} \\ \frac{\dot p_{i\perp}}{B} \\ \frac{\dot q_{i\perp}}{B}-c_{i\perp}^2\frac{\dot M_{i\|}}{B} \\ \frac{\dot p_{e\|}}{B} \\ \frac{\dot q_{e\|}}{B}-3c_{e\|}^2\frac{\dot M_{e\|}}{B} \\ \frac{\dot p_{e\perp}}{B} \\ \frac{\dot q_{e\perp}}{B}-c_{e\perp}^2\frac{\dot M_{e\|}}{B} \end{pmatrix}, \tag{6}$$

represents the effect of collisions; see [6] for more information about the collisional operators denoted by the dot accent marking, such as $\dot\rho$.

2.1. *Eigenvectors and Eigenvalues*

The characteristic-based schemes for the Euler equations, pioneered by Courant *et al.* [14] and Godunov [10], advance data from one time level to another by following characteristic lines in (x, t). Each wave in the system propagates at its own wave speed and thus can be identified with a particular characteristic. Godunov's scheme differs from those of Courant *et al.* in adopting the conservation form of the flow equations; in consequence it is suitable for flow containing shocks of any strength. Characteristic-based schemes make explicit use of intrinsic properties of the system of equations they approximate, so their formulation requires a careful analysis of the system.

The system of equations described by (1) has 10 distinct eigenmodes, each associated with a different wave speed (eigenvalues of **A**). As will be discussed in more detail later, the numerical technique requires transforming (1), by a change of state variables, into a system of equations where **A** is diagonal. For this transformed system, a linearized Riemann problem is solved at each cell interface; this serves to compute the fluxes of the original state quantities. This information is then used to advance (1) in time with a multi-stage scheme. The left and right eigenvectors of **A** are important, as they are used to transform to the diagonal system and back again. In this section we give approximate expressions for both the eigenvectors and the eigenvalues of **A**.

As shown by Gombosi and Rasmussen [6], the eigenvalues of **A** are

$$\begin{aligned} &\lambda_1=u+c_+, && \lambda_2=u-c_+, \\ &\lambda_3=u+c_-, && \lambda_4=u-c_-, \\ &\lambda_5=u+c_{i\|}, && \lambda_6=u-c_{i\|}, \\ &\lambda_7=u+\sqrt{3}\,c_{e\|}, && \lambda_8=u-\sqrt{3}\,c_{e\|}, \\ &\lambda_9=u+c_{e\|}, && \lambda_{10}=u-c_{e\|}, \end{aligned} \tag{7}$$

where

$$c_\pm=\sqrt{(\chi c_{e\|}^2+6c_{i\|}^2\pm\sqrt{\chi^2c_{e\|}^4+24c_{i\|}^4})/2}. \tag{8}$$

Of the eigenvalues given in (7), only $\lambda_{5,6,9,10}$ are exact. The other eigenvalues are approximate, with $\lambda_{7,8}$ valid for small values of χ (a good approximation) and $\lambda_{1,2,3,4}$ valid in the limit of very small heat fluxes q (not always guaranteed, as shown later). These formulas are intended to give an

idea of the scale of wave speeds encountered; in practice the eigenvalues are obtained numerically, without any approximation.

In general case, roots containing c_+ and c_- are the solutions of a fourth-order algebraic equation. As is shown in [9, 6], some of the eigenvalues can be complex in the case of very large heat flows. In these cases, however, the momentum expansion of the original distribution functions is not convergent and the equations are not valid anyhow. When the heat flows are extremely large, the distribution function corresponding to the flow parameters is negative in certain regions of the velocity space (see [6]), which signifies their unphysical nature. Although we cannot prove it generally, based on their asymptotic behavior in certain limits, we expect the eigenvalues to be real when the heat flows are reasonably small, namely $|q_{\|}| < p_{\|}^{3/2}/\rho^{1/2}$ and $|q_{\perp}| < p_{\perp}(p_{\|}/\rho)^{1/2}$. Our numerical experiments support this prediction. Thus, in cases of interest (1) represents a hyperbolic system of equations suited for initial-values problems. The problem of large heat flows is further investigated in the next section.

It is interesting to note that the eigenvalues are all distinct and evenly split about the flow velocity u. This differs from, e.g., the three-dimensional Euler equations, where three of the five eigenvalues are equal to u. The eigenvalues and eigenvectors can be degenerate for certain special combinations of flow parameters (e.g., when $T_{i\|} = T_{e\|}$ and $h_{i\|} = 0$ then $\lambda_3 = \lambda_5$ and $\lambda_4 = \lambda_6$) but there is no discontinuity around such points and the singularity can be removed by arbitrarily adding a very small pertuation to one of the flow parameters.

The state variables in the diagonal system of equations, also called "characteristic variables," will be denoted by $\hat{\mathbf{w}}$; they appear in the analysis only in differential form. The relation with the original state quantities can be written as

$$d\hat{\mathbf{w}} = \mathbf{U}^{-1}\, d\mathbf{w} \tag{9}$$

or, inversely,

$$d\mathbf{w} = \mathbf{U}\, d\hat{\mathbf{w}}, \tag{10}$$

where the matrices $\mathbf{U}$ and $\mathbf{U}^{-1}$ are composed of the right (column) eigenvectors and left (row) eigenvectors of $\mathbf{A}$, respectively. In other words, $d\hat{\mathbf{w}}$ is the projection of $d\mathbf{w}$ onto the right eigenvectors of $\mathbf{A}$; if we expand $d\mathbf{w}$ on the basis of the right eigenvectors, the elements of $d\hat{\mathbf{w}}$ are the expansion coefficients.

As the mapping from the original to the diagonal system of equations and vice versa is central to the numerical scheme presented here, the left and right eigenvectors performing this transformation are now given. The right eigenvectors are

$$U_{j1} = \begin{bmatrix} \rho \\ c_+ \\ \rho(c_+^2 - \chi c_{e\|}^2) \\ -\rho c_+(\chi c_{e\|}^2 - c_+^2 + 3c_{i\|}^2) \\ p_{i\perp} \\ 0 \\ p_{e\|} \\ -2c_+ p_{e\|} \\ p_{e\perp} \\ 0 \end{bmatrix}, \quad U_{j2} = \begin{bmatrix} \rho \\ -c_+ \\ \rho(c_+^2 - \chi c_{e\|}^2) \\ \rho c_+(\chi c_{e\|}^2 - c_+^2 + 3c_{i\|}^2) \\ p_{i\perp} \\ 0 \\ p_{e\|} \\ 2c_+ p_{e\|} \\ p_{e\perp} \\ 0 \end{bmatrix}, \tag{11a}$$

$$U_{j3} = \begin{bmatrix} \rho \\ c_- \\ \rho(c_-^2 - \chi c_{e\|}^2) \\ -\rho c_-(\chi c_{e\|}^2 - c_-^2 + 3c_{i\|}^2) \\ p_{i\perp} \\ 0 \\ p_{e\|} \\ -2c_- p_{e\|} \\ p_{e\perp} \\ 0 \end{bmatrix}, \quad U_{j4} = \begin{bmatrix} \rho \\ -c_- \\ \rho(c_-^2 - \chi c_{e\|}^2) \\ \rho c_-(\chi c_{e\|}^2 - c_-^2 + 3c_{i\|}^2) \\ p_{i\perp} \\ 0 \\ p_{e\|} \\ 2c_- p_{e\|} \\ p_{e\perp} \\ 0 \end{bmatrix}, \tag{11b}$$

$$U_{j5} = \begin{bmatrix} 0 \\ 0 \\ 0 \\ 0 \\ p_{i\perp} \\ c_{i\|} p_{i\perp} \\ 0 \\ 0 \\ 0 \\ 0 \end{bmatrix}, \quad U_{j6} = \begin{bmatrix} 0 \\ 0 \\ 0 \\ 0 \\ -p_{i\perp} \\ c_{i\|} p_{i\perp} \\ 0 \\ 0 \\ 0 \\ 0 \end{bmatrix}, \quad U_{j7} = \begin{bmatrix} 0 \\ \frac{\chi c_{e\|}}{\sqrt{3}} \\ 0 \\ 0 \\ 0 \\ 0 \\ p_{e\|} \\ \sqrt{3}\, c_{e\|} p_{e\|} \\ 0 \\ 0 \end{bmatrix}, \tag{11c}$$

$$U_{j8} = \begin{bmatrix} 0 \\ \frac{\chi c_{e\|}}{\sqrt{3}} \\ 0 \\ 0 \\ 0 \\ 0 \\ -p_{e\|} \\ \sqrt{3}\, c_{e\|} p_{e\|} \\ 0 \\ 0 \end{bmatrix}, \quad U_{j9} = \begin{bmatrix} 0 \\ 0 \\ 0 \\ 0 \\ 0 \\ 0 \\ 0 \\ p_{e\perp} \\ c_{e\|} p_{e\perp} \end{bmatrix}, \quad U_{j10} = \begin{bmatrix} 0 \\ 0 \\ 0 \\ 0 \\ 0 \\ 0 \\ 0 \\ -p_{e\perp} \\ c_{e\|} p_{e\perp} \end{bmatrix}. \tag{11d}$$

The left eigenvectors are

$$(U^{-1})_{1j} \propto \left(\frac{6c_{i\|}^2 - c_+^2}{2\rho c_{i\|}^2}, \frac{3c_{i\|}^2 - c_+^2}{2c_+ c_{i\|}^2}, \frac{-1}{2p_{i\|}}, \frac{-1}{2c_+ p_{i\|}}, 0, 0, 0, 0, 0, 0\right), \quad (12a)$$

$$(U^{-1})_{2j} \propto \left(\frac{6c_{i\|}^2 - c_+^2}{2\rho c_{i\|}^2}, \frac{-3c_{i\|}^2 + c_+^2}{2c_+ c_{i\|}^2}, \frac{-1}{2p_{i\|}}, \frac{1}{2c_+ p_{i\|}}, 0, 0, 0, 0, 0, 0\right), \quad (12b)$$

$$(U^{-1})_{3j} \propto \left(\frac{6c_{i\|}^2 - c_-^2}{2\rho c_{i\|}^2}, \frac{3c_{i\|}^2 - c_-^2}{2c_- c_{i\|}^2}, \frac{-1}{2p_{i\|}}, \frac{-1}{2c_- p_{i\|}}, 0, 0, 0, 0, 0, 0\right), \quad (12c)$$

$$(U^{-1})_{j4} \propto \left(\frac{6c_{i\|}^2 - c_-^2}{2\rho c_{i\|}^2}, \frac{-3c_{i\|}^2 + c^2}{2c_- c_{i\|}^2}, \frac{-1}{2p_{i\|}}, \frac{1}{2c_- p_{i\|}}, 0, 0, 0, 0, 0, 0\right), \quad (12d)$$

$$(U^{-1})_{5j} \propto \left(\frac{-1}{2\rho}, 0, 0, 0, \frac{1}{2p_{i\perp}}, \frac{1}{2c_{i\|} p_{i\perp}}, 0, 0, 0, 0\right), \quad (12e)$$

$$(U^{-1})_{6j} \propto \left(\frac{1}{2\rho}, 0, 0, 0, \frac{-1}{2p_{i\perp}}, \frac{1}{2c_{i\|} p_{i\perp}}, 0, 0, 0, 0\right), \quad (12f)$$

$$(U^{-1})_{7j} \propto \left(\frac{-1}{2\rho}, 0, 0, 0, 0, 0, \frac{1}{2p_{e\|}}, \frac{1}{\sqrt{12}\, c_{e\|} p_{e\|}}, 0, 0\right), \quad (12g)$$

$$(U^{-1})_{8j} \propto \left(\frac{1}{2\rho}, 0, 0, 0, 0, 0, \frac{-1}{2p_{e\|}}, \frac{1}{\sqrt{12}\, c_{e\|} p_{e\|}}, 0, 0\right), \quad (12h)$$

$$(U^{-1})_{9j} \propto \left(\frac{-1}{2\rho}, 0, 0, 0, 0, 0, 0, 0, \frac{1}{2p_{e\perp}}, \frac{1}{2c_{e\|} p_{e\|}}\right), \quad (12i)$$

$$(U^{-1})_{10j} \propto \left(\frac{1}{2\rho}, 0, 0, 0, 0, 0, 0, 0, \frac{-1}{2p_{e\perp}}, \frac{1}{2c_{e\|} p_{e\perp}}\right). \quad (12j)$$

We have not normalized the system of eigenvectors as we need the relative values only. Just as the eigenvalues, not all of the above eigenvectors are exact; the same approximations used to obtain the eigenvalues (7) were used to obtain the eigenvectors. In practice, both eigenvalues and eigenvectors are obtained numerically to ensure accuracy, particularly when heat fluxes are not small.

2.2. *Heat Fluxes*

A physical argument can be made that the moment expansions of Boltzmann's equation represented by (1) are valid only if the absolute values of the heat fluxes are smaller than a certain limit [6]. Above that limit, the positivity of the distribution function corresponding to the state variables is not guaranteed. For instance, the normalized heat flux,

$$h_{i\|} = q_{i\|}/c_{i\|} p_{i\|}, \quad (13)$$

must remain less than unity in order for (1) to be valid. This is problematic because there is nothing contained in the generalized transport equations to insure that this occurs. In fact, Palmadesso *et al.* [9] have solved (1) numerically and found that normalized ion heat fluxes can grow to quantities of order one and larger. One possible explanation for this is that wave propagation in the perpendicular heat fluxes is unphysical [9]. These ion waves correspond to the normal modes $\hat{w}_5$ and $\hat{w}_6$ described above.

In order to numerically test how accurately the above set of transport equations describes a physical problem, one must be assured that there are no numerical difficulties, that, by themselves, could lead to an excessive growth of the heat fluxes. One possibility for an excessive heat flux is that a change or perturbation $\Delta \mathbf{w}$ in one of the components of the state vector leads directly to an excessive change in one of the heat fluxes. This possibility is now considered.

By (10) we know that a variation in the perpendicular component of the electron heat flux, $q_{e\perp}$, for instance, can be expressed in terms of the characteristic variables by

$$\Delta w_{10} = \sum_{j=1}^{10} U_{10j}\, \Delta \hat{w}_j. \quad (14)$$

From (11) it is seen that only the elements $U_{10,9}$ and $U_{10,10}$ are nonzero, so only the eigenmodes $\hat{w}_9$ and $\hat{w}_{10}$ contribute to jumps in $q_{e\perp}$. Furthermore, from (9) and (11), in particular, from $(U^{-1})_{9j}$ and $(U^{-1})_{10j}$, which have non-zero elements only for $j = 1, 9, 10$, it follows that changes in $\hat{w}_9$ and $\hat{w}_{10}$ depend only on changes in ρ, $p_{e\perp}$, and $q_{e\perp}$ (actually, only on $T_{e\perp}$ and $q_{e\perp}$).

This linkage is shown graphically in Fig. 1. Any oscillation in, for instance, $p_{e\perp}$ (in the first column of the figure), excites eigenmodes $\hat{w}_9$ and $\hat{w}_{10}$ (in the second column). This

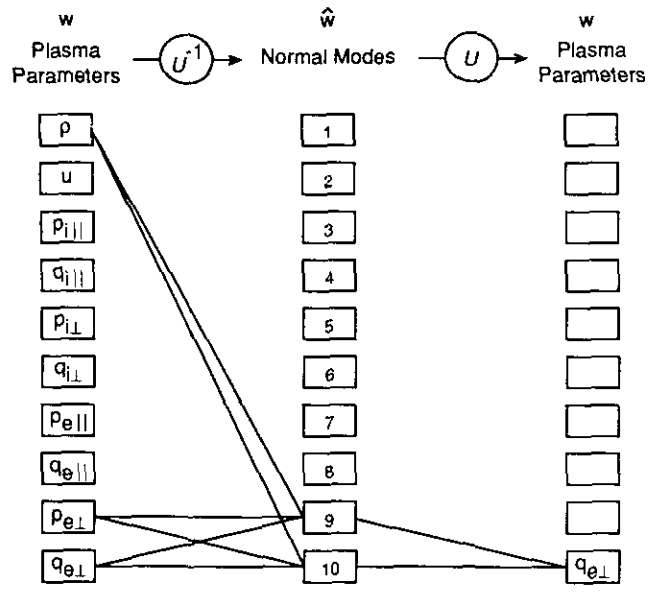

FIG. 1. Partial coupling of the eigenmodes and plasma parameters. A perturbation in $p_{e\perp}$ is ultimately coupled to $q_{e\perp}$ through the eigenmodes $\hat{w}_9$ and $\hat{w}_{10}$. The transformations between representations are noted by the matrix operators U^{-1} and U.

coupling is described by the matrix of left eigenvectors U^{-1}. These eigenmodes will in turn excite $q_{e\perp}$, as shown on the right-hand side of the figure. Quantitatively, from (14),

$$\Delta q_{e\perp} \equiv \Delta w_{10} = c_{e||}\, p_{e\perp}\, \Delta \hat{w}_9 + c_{e||}\, p_{e\perp}\, \hat{w}_{10}. \tag{15}$$

In order to insure that the normalized heat flux $h_{e\perp}$ remains small, a necessary condition is that $\Delta \hat{w}_9 \ll 1$. The same condition must be put on $\Delta \hat{w}_{10}$. From (9) and (11) it follows directly that

$$\Delta \hat{w}_9 = \frac{\Delta T_{e\perp}}{2T_{e\perp}} + \frac{\Delta q_{e\perp}}{2c_{e||}\, p_{e\perp}}. \tag{16}$$

Thus, we must require that relative changes in the perpendicular component of electron temperature, $\Delta T_{e\perp}/T_{e\perp}$, be much less than one.

An examination of perturbations in the other heat fluxes leads to similar conclusions: as long as relative changes in all of the components of **w** other than heat fluxes remain much less than one, then changes in heat flux will be limited accordingly. Of course, the influence of boundary conditions and internal sources will also affect the heat flux will be limited accordingly. Of course, the influence of boundary conditions and internal sources will also affect the heat flux, but these effects can be considered separately. For now, we require that the magnitude of perturbations be small and that the numerical simulation of wave propagation faithfully reproduces the coupling represented by the eigenvectors in (11) and (12). In the next section we describe a numerical scheme to perform precisely this task.

3. NUMERICAL METHOD

In this section we develop a Godunov-type higher-order scheme for the plasma transport equations. In particular, the spatial discretization of the equations follows that of a Godunov-type scheme such as MUSCL [11] or PPM [15]. The time discretization, though, is done differently, namely, by following the "method of lines" commonly used for integrating ordinary differential equations. This makes the space-time discretization modular, allowing considerable flexibility in the choice of components.

3.1. *Spatial Discretization*

In a Godunov-type scheme, the distribution of flow variables inside each computational cell is reconstructed with the aid of cell-averaged values in the neighboring cells. This leaves a discontinuity in the overall interpolant at each cell interface. Starting from such initial values, it becomes necessary to compute, exactly or in some approximation, the breakdown of each discontinuity, that is, to solve Riemann's initial-value problem with the two interface states as input states. In regular hydrodynamics, where the equations can be fully written in the conservation form, this step results in a unique set of interface fluxes for all of the state variable; these contain all the information needed for the temporal integration.

For the present set of equations the above approach must be modified, as it is not possible to write the system (1) entirely in the form of conservation equations. The culprit is the ambipolar electric field, which couples the ion and electron fluids; it introduces terms that are not total derivatives. This does not mean that electric energy does not satisfy a conservation principle; it just means that, at a discontinuity, ions and electrons do not conserve energy separately: the electric field transfers energy between them. In other words, there are fewer jump equations than variables. The transfer of energy is determined by the fine-scale structure of the so-called discontinuity, which in reality is not infinitely thin.

It must be emphasized that the present technique does not attempt to resolve the detailed transfer inside the thin layer. Instead, it relies on knowledge of all speeds of finite-amplitude waves, even if some of these do not arise from jump equations. It follows that properly simulating the waves is of the greatest importance.

A common approach to the discretization of non-conservative terms is to regard them as source terms instead of contributions to the fluxes—it is done routinely in *flux-corrected transport* methods [16]. It is precisely this approach that would lead to building incorrect wave speeds into the approximate Riemann solver and jeopardize the

ability of the method to properly represent the physics. The technique proposed below is a refined version of the one used by Kőrösmezey *et al* [17].

For the subcell reconstruction of state variables quadratic interpolation is used [12], subject to limiting of derivatives as suggested by Koren [19]. When interpolating smooth data, the interpolation is essentially quadratic, allowing a third-order accurate updating scheme. The limiter prevents interpolation across a discontinuity, thus preventing numerical oscillations. Suppose we are interpolating some conservative state variable W_k in cell i, using its average values $\bar{W}_{k,i}$, $\bar{W}_{k,i-1}$, and $\bar{W}_{k,i+1}$ in cells i, $i-1$, and $i+1$, respectively. The limiter is a scalar funcion $\psi(R)$; its argument R represents the rate of change of the solution's derivative,

$$R_{k,i}=\frac{(x_i-x_{i-1})(\bar{W}_{k,i+1}-\bar{W}_{k,i})}{(x_{i+1}-x_i)(\bar{W}_{k,i}-\bar{W}_{k,i-1})}. \tag{17}$$

The interpolant of W_k in cell i is the quadratic function whose cell average equals $\bar{W}_{k,i}$ and whose interface values are

$$\begin{aligned} W_k(x_{i-1/2+})&=\bar{W}_{k,i}-\frac{1}{2}\psi\left(\frac{1}{R_{k,i}}\right)(\bar{W}_{k,i+1}-\bar{W}_{k,i}),\\ W_k(x_{i+1/2-})&=\bar{W}_{k,i}+\frac{1}{2}\psi(R_{k,i})(\bar{W}_{k,i}-\bar{W}_{k,i-1}). \end{aligned} \tag{18}$$

For more information about the method of interpolation, see Appendix A. Koren's choice of ψ is

$$\psi(R)=\frac{2R^2+R}{2R^2-R+2}. \tag{19}$$

For smooth data, i.e., $R\approx 1$, this function is approximately $\frac{1}{3}+\frac{2}{3}R$, corresponding to quadratic interpolation consistent with the cell averages $W_k^{(i)}$, $W_k^{(i-1)}$, and $W_k^{(i+1)}$, without limiting.

Consider now the almost conservative form of the equations; this can be written as

$$\frac{\partial \mathbf{W}}{\partial t}+\frac{\partial \mathbf{F}}{\partial x}+\mathbf{L}\frac{\partial \mathbf{W}}{\partial x}=\mathbf{S}. \tag{20}$$

Here $\mathbf{W}$ is the vector of conserved state variables (the actual choice of these variables is specified in Appendix B) and $\mathbf{F}$ is the corresponding flux vector; the conservation form is spoiled by the term with the matrix coefficient $\mathbf{L}$, which cannot be written as a flux derivative. Introducing the flux Jacobian

$$\mathbf{K}=\frac{\partial \mathbf{F}}{\partial \mathbf{W}}, \tag{21}$$

we may write (20) as

$$\frac{\partial \mathbf{W}}{\partial t}+\mathbf{K}\frac{\partial \mathbf{W}}{\partial x}+\mathbf{L}\frac{\partial \mathbf{W}}{\partial x}=\mathbf{S} \tag{22}$$

or

$$\frac{\partial \mathbf{W}}{\partial t}+\mathbf{M}\frac{\partial \mathbf{W}}{\partial x}=\mathbf{S}, \tag{23}$$

with

$$\mathbf{M}=\mathbf{K}+\mathbf{L}. \tag{24}$$

The matrix $\mathbf{M}$ relates to the matrix $\mathbf{A}$ in (1) by a similarity transformation; its eigenvalues are the wave speeds presented in Section 2.1.

The time-marching scheme, for which we shall choose an explicit multi-stage scheme, updates the cell average $\mathbf{W}$, and therefore requires knowledge of $\partial \mathbf{W}/\partial t$. This time derivative must be evaluated *after* the resolution of the initial discontinuities (i.e., at $t+\delta t$), so that the effect of the waves moving into the cell from both sides is properly accounted

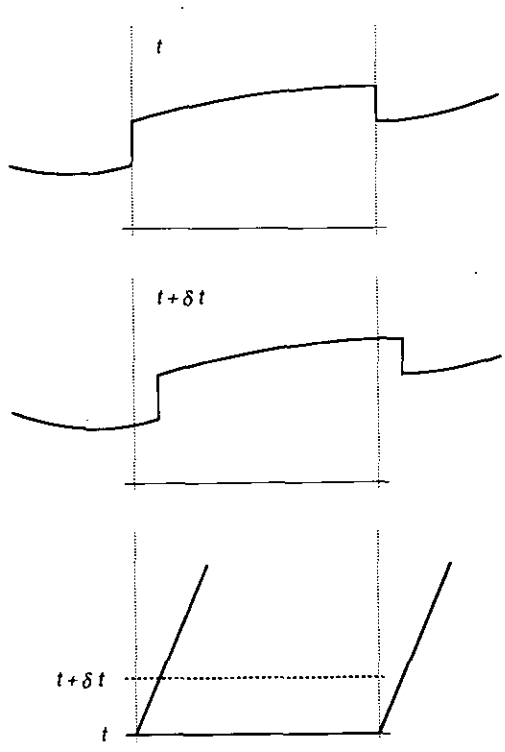

FIG. 2. Transport (by one right-going wave) of the discontinuities which occur at cell boundaries. The reconstructed solution at time t (top panel) is transported and shown at time $t+\delta t$ in the middle panel. Wave characteristics are shown in the bottom panel.

for; see Fig. 2. Averaging over cell i changes the system of equations into

$$\frac{\partial \bar{\mathbf{W}}_i}{\partial t} \equiv \frac{1}{\Delta x_i}\int_{x_{i-1/2}}^{x_{i+1/2}} \frac{\partial \mathbf{W}}{\partial t}\,dx = -\frac{1}{\Delta x_i}\left[\int_{x_{i-1/2}}^{x_{i+1/2}} \mathbf{M}\frac{\partial \mathbf{W}}{\partial x}\,dx - \int_{x_{i-1/2}}^{x_{i+1/2}} \mathbf{S}\,dx\right]_{t+\delta t}; \quad (25)$$

using a notation that is standard in describing upwind-difference schemes we obtain

$$\frac{\partial \bar{\mathbf{W}}_i}{\partial t} = -\frac{1}{\Delta x_i}\left[\int_{x_{i-1/2+}}^{x_{i+1/2-}} \mathbf{M}\frac{\partial \mathbf{W}}{\partial x}\,dx + \hat{\mathbf{M}}^+(\mathbf{W}_{i-1/2+} - \mathbf{W}_{i-1/2-}) + \hat{\mathbf{M}}^-(\mathbf{W}_{i+1/2+} - \mathbf{W}_{i+1/2-}) - \int_{x_{i-1/2+}}^{x_{i+1/2-}} \mathbf{S}\,dx\right]_t. \quad (26)$$

The matrix $\mathbf{M}^+$ is the "positive part" of $\mathbf{M}$: it has the same eigenvectors as $\mathbf{M}$ but has zero eigenvalues where $\mathbf{M}$ has negative eigenvalues. The "negative part" $\mathbf{M}^-$ is similarly defined. The matrix $\hat{\mathbf{M}}$ is evaluated at a cell interface using a special average $\hat{\mathbf{W}}$ of the interface values $\mathbf{W}_-$ and $\mathbf{W}_+$; using this average is advantageous because it yields a discrete form of Eq. (21),

$$\hat{\mathbf{K}}\,\Delta\mathbf{W} = \Delta\mathbf{F}; \quad (27)$$

see Roe [13]. Using this equation and the relations

$$\mathbf{M}^+ = \tfrac{1}{2}(\mathbf{M} + |\mathbf{M}|), \quad (28a)$$

$$\mathbf{M}^- = \tfrac{1}{2}(\mathbf{M} - |\mathbf{M}|), \quad (28b)$$

we can reduce the update equation to

$$\frac{\partial \bar{\mathbf{W}}_i}{\partial t} = -\frac{1}{\Delta x_i}\left[\mathbf{F}_{i+1/2} - \mathbf{F}_{i-1/2} + \int_{x_{i-1/2+}}^{x_{i+1/2-}} \mathbf{L}\times\frac{\partial \mathbf{W}}{\partial x}\,dx - \int_{x_{i-1/2+}}^{x_{i+1/2-}} \mathbf{S}\,dx + \frac{1}{2}\hat{\mathbf{L}}_{i-1/2}(\mathbf{W}_{i-1/2+} - \mathbf{W}_{i-1/2-}) + \frac{1}{2}\hat{\mathbf{L}}_{i+1/2}(\mathbf{W}_{i+1/2+} - \mathbf{W}_{i+1/2-})\right]_t, \quad (29)$$

with

$$\mathbf{F}_{i\pm 1/2} = \tfrac{1}{2}(\mathbf{F}_{i\pm 1/2-} + \mathbf{F}_{i\pm 1/2+}) - \tfrac{1}{2}|\hat{\mathbf{M}}_{i\pm 1/2}|\,(\mathbf{W}_{i\pm 1/2+} - \mathbf{W}_{i\pm 1/2-}), \quad (30)$$

resembling the usual upwind-biased numerical flux-function.

The fact that the matrix $\mathbf{L}$ is not a flux derivative has the consequence that values of $\partial\mathbf{W}/\partial x$ in the interior of cell i appear explicitly. The cell integrals of $\mathbf{L}\,\partial\mathbf{W}/\partial x$ and $\mathbf{S}$ in practice are approximated by Simpson's formula, e.g.,

$$\int_{x_{i-1/2}}^{x_{i+1/2}} \mathbf{S}(x)\,dx \approx \frac{\Delta x_i}{6}[\mathbf{S}(x_{i-1/2+}) + 4\mathbf{S}(x_i) + \mathbf{S}(x_{i+1/2-})]; \quad (31)$$

the values of S or any other quantity inside the cell follow from the interpolant $W(x)$.

The variables belonging to the electron modes change much more smoothly spatially than those of the ions, due the strong heat conduction of electrons. To make the code more efficient electrons are represented on a four times cruder grid than the ions the electron variables are transferred by interpolation to the ion component's grid.

3.2. *Sources*

The generalized transport equations described above are applicable in a variety of different flow regimes. In one regime (near a planets' surface, for instance), reactive and collisional terms in the sources $\mathbf{S}$ may entirely dominate the time evolution of the solution. In other regimes (at high altitudes where densities are relatively low, for example), reactive and collisional terms in $\mathbf{S}$ may be negligible and the time evolution is dominated by transport. Frequently the reactive time scales are much shorter than the transport time scales in at least a portion of the region being modeled. This disparate variety of time scales slows down the numerical solution unless proper techniques are utilized to deal with the stiffness.

We first examine the strongly reactive regime to examine potential ways to speed up the numerical solution. In this parameter regime transport can be neglected entirely and the source terms are split into two components. For instance, the conservation equation describing the evolution of mass density per unit magnetic flux W_1 can be written as

$$\frac{\partial W_1}{\partial t} = S_1 = -\nu_1 W_1 + \tilde{S}_1, \quad (32)$$

where ν_1 is a loss frequency describing the rate at which mass is lost due to the recombination of ions with electrons. In (32), source terms which are independent of the flow parameters $\mathbf{W}$ (for instance, terms describing the production of mass due to photoionization of a neutral species) are

contained in $\tilde{S}_1$. Note that ν_1 and $\tilde{S}_1$ are assumed to be constant in time. Equation (32) then has the exact solution,

$$W_1(t+\Delta t) = W_1(t) + \left(\frac{\tilde{S}_1}{\nu_1} - W_1(t)\right)(1 - e^{-\nu_1 \Delta t}), \quad (33)$$

which we exploit to develop a numerical scheme to advance W_1 in time,

$$\begin{aligned} \delta W_1 &= W_1(t+\Delta t) - W_1(t) \\ &= \left(\frac{\tilde{S}_1}{\nu_1} - W_1(t)\right)(1 - e^{-\nu_1 \Delta t}). \end{aligned} \quad (34)$$

For $\nu_1 \Delta t \ll 1$, Eq. (34) can be expanded in a Taylor's series to obtain

$$\delta W_1 \simeq \nu_1 \Delta t \left(\frac{\tilde{S}_1}{\nu_1} - W_1(t)\right), \quad (35)$$

with a truncation error of order $(\Delta t)^2$. It is noted that (35) is just Euler's method for advancing (32) forward in time. In the other extreme, $\nu_1 \Delta t \gg 1$, the change in W_1 is

$$\delta W_1 \simeq \left(\frac{\tilde{S}_1}{\nu_1} - W_1(t)\right) \quad (36)$$

and W_1 reaches the steady-state solution of (32) in one time step. Thus, it is seen that the exponential term on the right-hand side of (34) acts as a limiter to reduce the change in W_1 which can occur in a single time step.

The exponential limiter in (34) is used to stabilize the numerical solution when Δt is allowed to be of the order of ν_1 or greater. It stabilizes the solution but it must be used with caution. It was observed that the numerical solution converges to a wrong steady state in some instances when operator splitting was used to combine the transport terms with the exponential growth and decay described by (32). We have found that, in general, the full effects of transport must be included in the $\tilde{S}_1$ term in (34) in order for the solution to converge to the correct steady state.

3.3. *Time Marching*

The characteristic time scale of the electron component is much shorter than that of the ions. Despite the fact that we are using a four times larger grid spacing for electrons, the electron modes require much smaller time-step sizes than the ion modes. To improve the efficiency of the code we employ the method of "time-splitting." First the ion modes are advanced by a time step Δt, then the fast electron modes are advanced by $2\Delta t$ in several steps of a smaller size, and finally another ion step of Δt is performed.

The time integration of the ion equations was carried out by the "method of lines." The third-order scheme of Shu and Osher [20] is used. If T is the operator advancing the variable $\mathbf{W}$ by Δt,

$$\mathbf{W}(t+\Delta t) = T(\mathbf{W}(t)), \quad (37)$$

the scheme takes the form

$$\begin{aligned} \mathbf{W}^{(1)} &= T(\mathbf{W}^{(0)}), \\ \mathbf{W}^{(2)} &= \tfrac{3}{4}\mathbf{W}^{(0)} + \tfrac{1}{4}T(\mathbf{W}^{(1)}), \\ \mathbf{W}^{(3)} &= \tfrac{1}{3}\mathbf{W}^{(0)} + \tfrac{2}{3}T(\mathbf{W}^{(2)}). \end{aligned} \quad (38)$$

Here the superscripts denote the level of iteration, level 3 is the end result after a time step Δt. The particular advantage of this choice is that only the values of the previous level have to be stored in addition to $\mathbf{W}^{(0)}$. The individual time-steps of the electron modes are calculated only with first-order accuracy but, because there are about 10 electron steps during one ion step, this provides at least the same temporal accuracy as that of the ions on the scale of Δt. According to [21] this "time-splitting" scheme provides at least second-order accuracy but, as electrons reach equilibrium relatively quickly, an accuracy closer to third order can be expected.

Let us summarize here the substeps which each evaluation of T in (38) and in each electron time step includes:

- First, the actual values of the flow parameters and their gradients at cell interfaces and in the middle of each cell are reconstructed from the cell-averaged values by means of the interpolants (Eqs. (18), (A3)).
- The contribution of $\mathbf{M} \cdot (\partial \mathbf{W}/\partial x)$ is calculated by means of the generalized Riemann solver (terms in (29) containing $\mathbf{F}$ or $\mathbf{L}$).
- The sources $\mathbf{L} \cdot (\partial \mathbf{W}/\partial x)$ and $\mathbf{S}$ are evaluated at cell interfaces and at cell midpoints and are combined by the use of Simpson's formula (31).
- Using (29) the cell-averaged values are updated from time t to $t + \Delta t$.

4. EXAMPLE SOLUTIONS

The numerical scheme discussed above has been implemented in a computer program and various tests have been made. Numerical solutions to (1) are now shown for two simple cases. In each of these examples, all sources terms have been neglected. In particular, the assumption that spatial derivatives of the magnetic field are negligible (see (4)), implies that the area of the confining magnetic flux tube is constant and removes coupling of wave modes which are solely due to geometrical considerations. Neglect of the source terms allows a clear demonstration of the decoupling

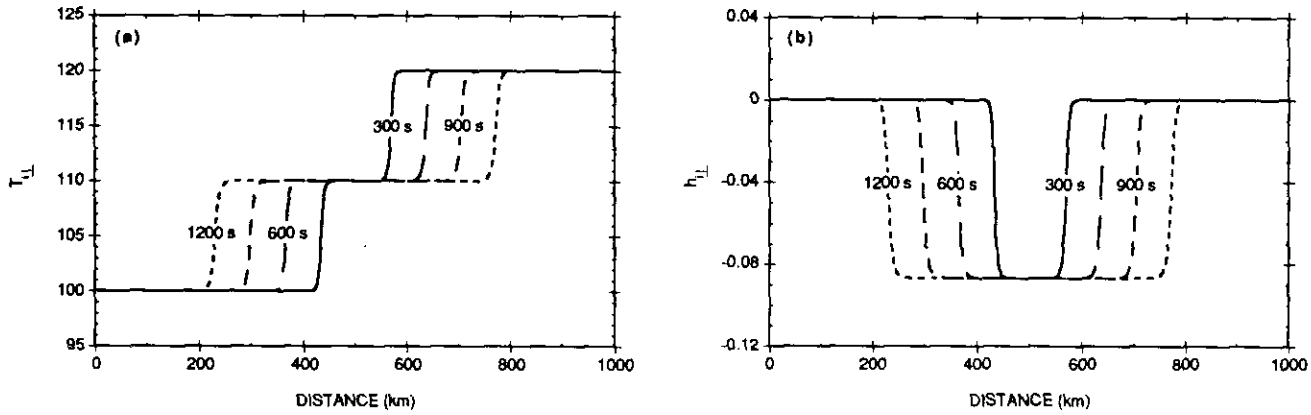

FIG. 3. Propagation of the ion thermal-heat wave for an initial 20% jump in ion temperature $T_{i\perp}$ at $x = 500$ km. One left-going wave and one right-going wave were excited. Perpendicular temperature is plotted in (a) and normalized heat flux ($h_{i\perp} = q_{i\perp}/c_{i\parallel}/p_{i\perp}$ in (b). Times at which various curves are plotted are shown in seconds.

of the different types of propagating waves. In the two cases considered here, unperturbed density and temperatures were $n = 100\ \text{cm}^{-3}$ and $T_{e\parallel} = 3T_{i\parallel} = 300$ K. Velocity and heat fluxes were initially zero. The spatial step size used for the tests was approximately 4 km and the Courant number of the fastest wave was 0.8.

The propagation of the ion thermal-heat wave is shown in Fig. 3. In this example, two simple waves were excited by an initial step jump in perpendicular ion temperature at $x = 500$ km. The magnitude of the temperature jump was 20 K (20% of the background). Both a left- and right-going wave are noted in Fig. 3a, traveling away from the location of the initial temperature jump with a speed of $c_{i\parallel} \simeq 0.23$ km/s (see values given for λ_5 and λ_6 in (7)). The spatial grid size was 4 km. The four times at which curves are plotted are $t = 300$, 600, 900, and 1200 s, where an interval of 300 s is about 20 time steps.

Using the right and left eigenvectors given in Eqs. (11) and (12), it can easily be shown that $\Delta h_{i\perp} \simeq \Delta T_{i\perp}/T_{i\perp} = 0.091$ (the later is obtained from Fig. (3a). This value accurately compares with the jumps in perpendicular heat flux calculated by the numerical model and displayed in Fig. 3b. While perpendicular heat flux perturbations are expected to be excited by the initial temperature jump (due to the coupling which occurs via eigenmodes $\hat{w}_5$ and $\hat{w}_6$), other plasma parameters are not affected and therefore are not plotted. In particular, mass and momentum perturbations did not occur in this example, as expected.

Numerical damping of the high-frequency components of the waves is evident in Fig. 3, as the initial sharp jump in temperature no longer occurs over the width of one cell. By $t = 300$ s the transition region has broadened somewhat, so that the jump takes place over about six cells or a distance of approximately 25 km. After this time the width of the transition region increases only slightly, so that by 900 s the jump takes place in about seven cells.

The propagation of the ion-acoustic mode is shown in Fig. 4. In this example, four simple waves wre excited by an initial 20% density enhancement over two cells at the center of the spatial grid. (The grid size is 2 km in this model run.) Two of these waves propagate to the left and two to the right at speeds given by the first four eigenvalues, $\lambda_{1,2,3,4}$, in (7). For the background values listed above, the propagation speeds for the fast and slow modes are 0.617 km/s and 0.290 km/s, respectively, and were very accurately reproduced in the numerical solution. The density perturbations seen in Fig. 4a are coupled through the first four eigenmodes to velocity, parallel temperature, and parallel heat flux. Thus, perturbations occur in these quantities as well, as can be seen in Figs. 4b–d. Excitation of the ion thermal-heat wave shown in Fig. 3 did not occur in this test, as expected.

While the wave speeds are faithfully represented, the wave forms are difficult to describe numerically because of the broad Fourier spectrum needed to describe a narrow square pulse. After 300 s (Fig. 4a) damping of the high-frequency end of the spectrum has already significantly broadened and attenuated the pulses. The half-width of the fastest moving pulses has increased to 11 cells, the slower pulses are eight cells wide. In order to ensure conservation the amplitude of the perturbation decreases correspondingly. During the propagation of the waves it was found that the total mass in the modeled region was conserved to within 1–2%.

Examples of the ion modes have been shown only. Electron modes are somewhat different from the ions, primarily because of their much higher wave speeds. The electrons have both a parallel and a perpendicular thermal-heat wave, in contrast to the ions, where only the perpendicular components are thermal-heat waves. In the case of the ions, parallel temperature and heat flux are coupled to mass and momentum perturbations to form the ion acoustic wave. Mass and momentum perturbations (which are carried by the ions) are simply too slow and ponderous to be affected

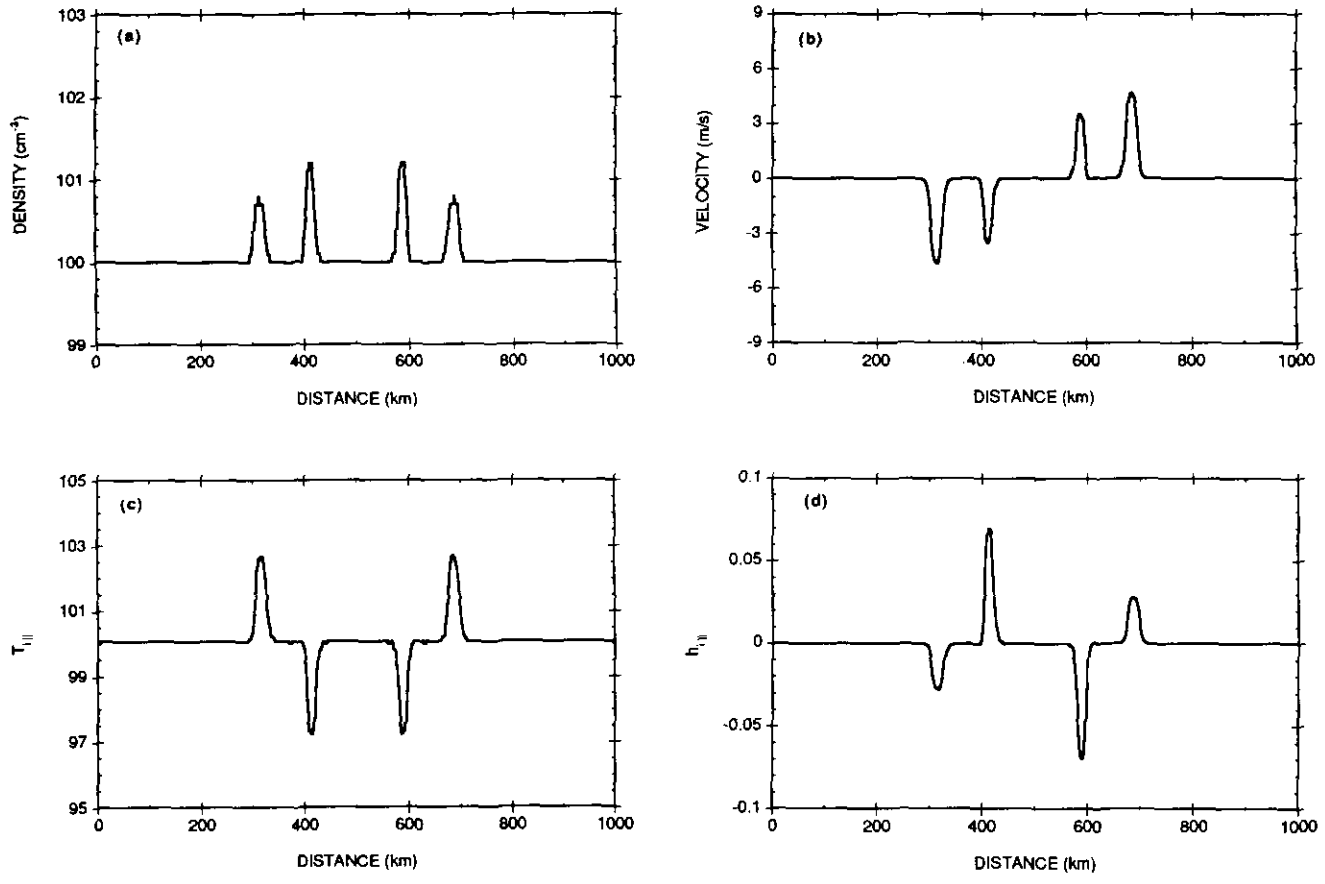

FIG. 4. The ion-acoustic wave at $t = 300$ s for an initial 20% increase in ion density at the two cells centered about $x = 500$ km. Two left-going waves (one slow and one fast) and two right-going waves were excited. Ion density is plotted in (a), velocity in (b), parallel temperature in (c), and normalized heat flux ($h_{i\|} = q_{i\|}/c_{i\|}/p_{i\|}$ in (d)).

by the much faster parallel electron perturbations. The electron modes are solved on a grid with an increased step size (in order to allow the time step not to be excessively small); results for the electron thermal-heat waves are similar to the ion waves shown in Fig. 3 and are not shown here.

The above examples demonstrate the scheme's correct behavior in the linear regime. Showing more complex calculations is beyond the scope of the present paper. For the first "real world" application of the scheme see [18], where O^+ ion outflow is modeled along a magnetic flux tube in the Earth's ionosphere and the temporal development of disturbances in the flux is caused by magnetic storms.

5. CONCLUSIONS

A numerical solution to the 16-moment set of transport equations has been found which employs a high-order Godunov scheme to achieve third-order accuracy in space and second-order accuracy in time. A modification of the "approximate Riemann solver" of Roe [13] was necessary because the electric-field term, coupling the ion and electron species, made it impossible to write the relevant set of equations in strict conservation form. In addition, a new technique has been developed to overcome the stiffness that occurs in regions where plasmas flows are strongly reactive.

The 16-moment set of generalized transport equations form a complicated hyperbolic initial-value problem. While these equations have been solved previously for a plasma embedded in a strong magnetic field, problems relating to an uncontrolled growth in heat flux have been reported [9]. We have shown that perturbations in heat flux remain properly bounded as long as relative perturbations in other parameters are also small, e.g., $\Delta T_\perp/T_\perp \ll 1$. This conclusion has been supported by our numerical results.

APPENDIX A: INTERPOLATION FORMULAE

The Taylor expansion of the variables $\mathbf{W}$ around x_i is

$$\mathbf{W}(x) = \mathbf{W}(x_i) + \frac{\partial \mathbf{W}}{\partial x}(x_i)(x - x_i) + \frac{1}{2}\frac{\partial^2 \mathbf{W}}{\partial x^2}(x_i)(x - x_i)^2 + O(\Delta x^3). \quad \text{(A1)}$$

Using this interpolation inside the cell containing x_i the cell-average of $\mathbf{W}(x)$ is

$$\bar{\mathbf{W}}_i = \frac{1}{\Delta x}\int_{x_{i-1/2}}^{x_{i+1/2}} \mathbf{W}(x)\,dx = \mathbf{W}(x_i) + \frac{1}{24}\frac{\partial^2 \mathbf{W}}{\partial x^2}(x_i)\,\Delta x^2 + O(\Delta x^4). \quad \text{(A2)}$$

We can then express $\mathbf{W}(x)$ in terms of the cell-averaged quantities,

$$\mathbf{W}(x) = \bar{\mathbf{W}}_i + \partial_x \bar{\mathbf{W}}(x_i)(x-x_i) + \tfrac{1}{2}\partial_x^2 \bar{\mathbf{W}}[(x-x_i)^2 - \tfrac{1}{12}(\Delta x)^2] + O(\Delta x^3), \quad \text{(A3)}$$

where $\partial_x \bar{\mathbf{W}}(x_i)$ and $\partial_x^2 \bar{\mathbf{W}}$ are the derivatives calculated using finite differences. For an equidistant grid, a possible choice for these could be

$$\partial_x \bar{\mathbf{W}}(x_i) = \frac{1}{2\Delta x}(\bar{\mathbf{W}}_{i+1} - \bar{\mathbf{W}}_{i-1})$$
$$\partial_x^2 \bar{\mathbf{W}}(x_i) = \frac{1}{\Delta x^2}(\bar{\mathbf{W}}_{i+1} - 2\bar{\mathbf{W}}_i + \bar{\mathbf{W}}_{i-1}). \quad \text{(A4)}$$

As is mentioned in Section 3.1 we use piecewise parabolic interpolation with the limiter function of Koren [19] instead of (A4). With the use of the limiter the scheme is third-order accurate spatially in regions where the flow variables change smoothly, but in regions of sharp changes (e.g., at shock boundaries) it changes from using centered quadratic interpolation to one-sided linear interpolation. In this way we avoid differencing across a shock transition, thus preventing numerical oscillations.

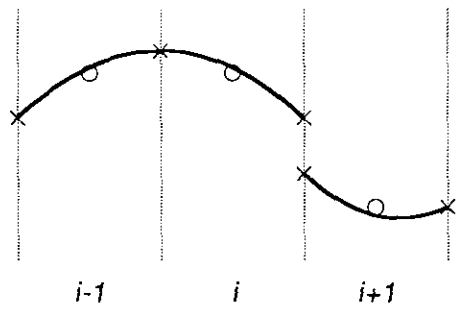

FIG. 5. Polynomial interpolation of cell average quantities. The vertical dashed lines denote the location of cell boundaries, circles represent cell averages, and crosses represent interpolated quantities at the cell boundaries.

Another complication arises from the use of a non-equidistant grid. Figure 5 shows the piecewise parabolic interpolant. Using this approach, the expression for $\mathbf{W}(x)$ is

$$\begin{aligned}\mathbf{W}(x) = \bar{\mathbf{W}}_i &- \frac{1}{8}\left[\frac{\Delta_-}{\Delta_+}\psi(R_i^{-1})(\bar{\mathbf{W}}_{i+1} - \bar{\mathbf{W}}_i) - \frac{\Delta_+}{\Delta_-}\psi(R_i)(\bar{\mathbf{W}}_i - \bar{\mathbf{W}}_{i-1})\right] \\ &+ \frac{1}{2\Delta x}\left[\frac{\Delta_-}{\Delta_+}\psi(R_i^{-1})(\bar{\mathbf{W}}_{i+1} - \bar{\mathbf{W}}_i) + \frac{\Delta_+}{\Delta_-}\psi(R_i^{-1})(\bar{\mathbf{W}}_i - \bar{\mathbf{W}}_{i-1})\right](x-x_i) \\ &- \frac{3}{2\Delta x^2}\left[\frac{\Delta_-}{\Delta_+}\psi(R_i^{-1})(\bar{\mathbf{W}}_{i+1} - \bar{\mathbf{W}}_i) - \frac{\Delta_+}{\Delta_-}\psi(R_i)(\bar{\mathbf{W}}_i - \bar{\mathbf{W}}_{i-1})\right](x-x_i)^2,\end{aligned} \quad \text{(A5)}$$

where $\Delta_+ = x_{i+1} - x_i$, $\Delta_- = x_i - x_{i-1}$, and R_i and $\psi(R)$ is given by (17) and (19), respectively.

From (A5) we can deduce that, instead of (A4),

$$\begin{aligned}\partial_x \bar{\mathbf{W}}(x_i) &= \frac{1}{2\Delta x}\left[\frac{\Delta_-}{\Delta_+}\psi(R_i^{-1})(\bar{\mathbf{W}}_{i+1} - \bar{\mathbf{W}}_i) + \frac{\Delta_+}{\Delta_-}\psi(R_i)(\bar{\mathbf{W}}_i - \bar{\mathbf{W}}_{i-1})\right] \\ \partial_x^2 \bar{\mathbf{W}}(x_i) &= -\frac{3}{\Delta x^2}\left[\frac{\Delta_-}{\Delta_+}\psi(R_i^{-1})(\bar{\mathbf{W}}_{i+1} - \bar{\mathbf{W}}_i) - \frac{\Delta_+}{\Delta_-}\psi(R_i)(\bar{\mathbf{W}}_i - \bar{\mathbf{W}}_{i-1})\right]\end{aligned} \quad \text{(A6)}$$

and that (A5) is equivalent to the Taylor expansion (A3) using these derivatives. For an equidistant grid and smoothly changing regions $R_i \approx 1$, $\psi(R) \approx \frac{1}{3} + \frac{2}{3}R$, and (A5) converges to the result of the Taylor expansion (A3) with the derivatives (A4). Evaluating (A5) at the cell boundaries yields (18).

APPENDIX B: QUASI-CONSERVATIVE FORM OF EQUATIONS

Ion Equations

There are several possibilities to write the part of (1) that describes the ion component in the quasi-conservative form (23). The choice closest to the form of a conservation principle contains the derivatives of ρ only in non-conservative terms. The disadvantage of using this form is that the state variables containing heat fluxes contain additional terms

which, in certain instances, can be much larger than the actual heat fluxes. To avoid the numerical inaccuracy resulting from this we use the same choice as in Eq. (2) for these elements. The form we have chosen is the following: the flow variables are

$$\mathbf{W}^{(i)}=\frac{1}{B}(\rho,\ \rho u,\ \rho u^2+p_{i\|},\ p_{i\perp},\ q_{i\|},\ q_{i\perp})^{\mathrm{T}}; \tag{B1}$$

the conserved fluxes are

$$\mathbf{F}^{(i)}=\frac{1}{B}\begin{pmatrix} \rho u \\ \rho u^2+p_{i\|} \\ \rho u^3+3up_{i\|}+q_{i\|} \\ up_{i\perp}+q_{i\perp} \\ uq_{i\|}+\dfrac{3}{2}\dfrac{p_{i\|}^2}{\rho B} \\ uq_{i\perp}+\dfrac{p_{i\|}p_{i\perp}}{\rho} \end{pmatrix}; \tag{B2}$$

and the non-zero elements of the matrix $\mathbf{L}$ are

$$\begin{aligned} L_{2,1}^{(i)}&=\chi c_e^2,\\ L_{3,1}^{(i)}&=2u\chi c_e^2,\\ L_{5,1}^{(i)}&=-3\left(\frac{1}{2}a_i^2+\frac{uq_{i\|}}{\rho}\right),\\ L_{5,2}^{(i)}&=\frac{q_{i\|}}{\rho},\\ L_{6,1}^{(i)}&=-\frac{u^2p_{i\perp}+uq_{i\perp}}{\rho},\\ L_{6,2}^{(i)}&=\frac{2up_{i\perp}+q_{i\perp}}{\rho},\\ L_{6,3}^{(i)}&=\frac{p_{i\perp}}{\rho}. \end{aligned} \tag{B3}$$

The form of the sources is

$$\begin{aligned} S_1^{(i)}&=\frac{\dot\rho}{B}-\frac{\rho}{B^2}\frac{D_\perp B}{Dt},\\ S_2^{(i)}&=\frac{\rho}{B}\frac{k}{m_i}\frac{\partial T_{e\|}}{\partial x}+\frac{\dot M_{i\|}+\dot M_{e\|}}{B}\\ &\quad+\frac{\dot\rho}{B}u+\frac{\rho}{B}g_{\|}-\frac{p_{i\perp}+p_{e\perp}}{B}\frac{1}{B}\frac{\partial B}{\partial x}\\ &\quad-\frac{\rho u}{B^2}\frac{D_\perp B}{Dt}+\frac{\rho}{B}u_\perp\left(\frac{D_\perp}{Dt}+u\frac{\partial}{\partial x}\right)\frac{\mathbf{B}}{B}, \end{aligned}$$

$$\begin{aligned} S_3^{(i)}&=2\frac{\rho}{B}u\frac{k}{m_i}\frac{\partial T_{e\|}}{\partial x}+\frac{\dot p_{i\|}}{B}\\ &\quad+2u\frac{\dot M_{i\|}+\dot M_{e\|}}{B}+\frac{\dot\rho}{B}u^2+2\frac{\rho}{B}ug_{\|}\\ &\quad-2\frac{u(p_{i\perp}+p_{e\perp})+q_{i\perp}}{B}\frac{1}{B}\frac{\partial B}{\partial x}\\ &\quad-\left(\frac{\rho}{B}u^2+\frac{p_{i\|}}{B}\right)\frac{1}{B}\frac{D_\perp B}{Dt}\\ &\quad+2\frac{\rho}{B}uu_\perp\left(\frac{D_\perp}{Dt}+u\frac{\partial}{\partial x}\right)\frac{\mathbf{B}}{B}+2\frac{p_{i\|}}{B}\frac{\mathbf{u}_\perp\cdot\mathbf{R}}{R^2}, \end{aligned} \tag{B4}$$

$$\begin{aligned} S_4^{(i)}&=\frac{\dot p_{i\perp}}{B}+\frac{up_{i\perp}+q_{i\perp}}{B}\frac{1}{B}\frac{\partial B}{\partial x}\\ &\quad-\frac{p_{i\perp}}{B}\left(\frac{1}{B}\frac{D_\perp B}{Dt}+\nabla\cdot\mathbf{u}_\perp+\frac{\mathbf{u}_\perp\cdot\mathbf{R}}{R^2}\right),\\ S_5^{(i)}&=\frac{\dot q_{i\|}}{B}-3\frac{p_{i\|}}{\rho}\frac{\dot M_{i\|}}{B}-\frac{q_{i\|}}{B}\left(\frac{1}{B}\frac{D_\perp B}{Dt}-3\frac{\mathbf{u}_\perp\cdot\mathbf{R}}{R^2}\right),\\ S_6^{(i)}&=\frac{\dot q_{i\perp}}{B}-\frac{p_{i\perp}}{\rho}\frac{\dot M_{i\|}}{B}-\frac{q_{i\perp}}{B}\left(\frac{1}{B}\frac{D_\perp B}{Dt}+\nabla\cdot\mathbf{u}_\perp\right)\\ &\quad+\left[u\frac{q_{i\perp}}{B}+c_{i\perp}^2\left(\frac{p_{i\|}}{B}-\frac{p_{i\perp}}{B}\right)\right]\frac{1}{B}\frac{\partial B}{\partial x}. \end{aligned}$$

There are derivatives of $T_{e\|}$ in the source terms; equations for the electron state variables are solved separately by time-splitting. For the averaging procedure at cell interfaces, Roe's averaging scheme [13] was used by introducing the new variables

$$\sqrt{\frac{\rho}{B}}\left(1,\ u,\ \frac{p_{i\|}}{\rho}+u^2,\ p_{i\perp},\ \frac{q_{i\|}}{\rho},\ \frac{q_{i\perp}}{\rho}\right)^{\mathrm{T}}. \tag{B5}$$

Unfortunately, as the nonlinearity of the equations is stronger than in usual hydrodynamics, there are a few terms in $\mathbf{W}$ and $\mathbf{F}$ that cannot be written as quadratic expressions in terms of the new variables; this introduces some deviation from the identity (27).

Electron Equations

The electron variables in $\mathbf{W}$ are defined as

$$\mathbf{W}^{(e)}=\frac{1}{B}(T_{e\|},\ T_{e\perp},\ q_{e\|},\ q_{e\perp}).$$

When transcribing the relevant equations from the set (1) to the form (20) the conservative part was chosen to be zero and all the spatial derivatives of the electron variables were

treated as non-conservative terms. In this way no terms have to be introduced to cancel the superfluous derivatives of ρ in the gradient of the fluxes (e.g., $(U^{-1})_{10,1}$ in $(12j)$). In the problems of interest the change in density may be large and the inaccuracy in this cancellation can deteriorate the solution.

The averaging procedure of Roe can be implemented by simply using $\mathbf{W}^{(e)}$ as the variable to average. The possible conservative fluxes (if we defined these) would be quadratic (mostly linear) functions of these.

ACKNOWLEDGMENT

This work was supported by the NASA Space Physics Theory Program under Grant NAGW-2162.

REFERENCES

1. G. F. Chew, M. L. Goldberger, and F. E. Low, *Proc. R. Soc. London Ser. A* **236**, 112 (1956).
2. V. Oraevskii, R. Chodura, and W Feneberg, *Plasma Phys.* **10**, 819 (1968).
3. J. M. Burgers, *Flow Equations for Composite Gases* (Academic Press, San Diego, CA, 1969).
4. A. R. Barakat and R. W. Schunk, *Plasma Phys.* **24**, 389 (1982).
5. V. N. Oraevskii, Y. V. Konikov, and G. V. Khazanov, *Transport Processes in Anisotropic Near-Earth Plasmas* (Nauka, Moscow, 1985). [Russian]
6. T. I. Gombosi and C. E. Rasmussen, *J. Geophys. Res.* **96**, 7759 (1991).
7. G. V. Khazanov, M. A. Koen, Y. V. Konikov, and I. M. Sidorov, *Planet. Space Sci.* **32** (1984), 585.
8. H. G. Mitchell, Jr. and P. J. Palmadesso, *J. Geophys. Res.* **88**, 2131 (1983).
9. P. J. Palmadesso, S. B. Ganguli, and H. G. Mitchell, Jr., in *Modeling Magnetospheric Plasma*, Geophys. Monogr. Ser., Vol. 44, edited by T. E. Moore and J. H. Waite (AGU, Washington, DC, 1988), p. 133.
10. S. K. Godunov, *Mat. Sb.* **47**, 357 (1959); also U. S. JPRS translation 7226, 1960.
11. B. van Leer, *J. Comput. Phys.* **23**, 276 (1977).
12. B. van Leer, *J. Comput. Phys.* **32**, 101 (1979).
13. P. L. Roe, *J. Comput. Phys.* **43**, 357 (1981).
14. R. Courant, E. Isaacson, and M. Rees, *Commun. Pure Appl. Math.* **5**, 243 (1952).
15. P. Colella and P. R. Woodward, *J. Comput. Phys.* **54**, 174 (1984).
16. D. L. Book, J. P. Boris, and K. H. Hain, *J. Comput. Phys.* **18**, 248 (1975).
17. Á. Kőrösmezey, J. Kim, and A. F. Nagy, *J. Geophys. Res.*, submitted.
18. Á. Kőrösmezey, C. E. Rasmussen, T. I. Gombosi, and G. V. Khazanov, *Geophys. Res. Lett.* **19**, 2289 (1992).
19. B. Koren, Ph.D. thesis, 1987.
20. C. W. Shu and S. Osher, *J. Comput. Phys.* **77** (1988), 439.
21. A. R. Gurlay and J. L. Morris, *J. Comput. Phys.* **5** (1970), 229.